nature nanotechnology
ARTICLES
https://doi.org/10.1038/s41565-020-0754-x

High quality factor phase gradient metasurfaces

Mark Lawrence[1,6] ✉, David R. Barton III[1,6] ✉, Jefferson Dixon[2], Jung-Hwan Song[3], Jorik van de Groep[3,5], Mark L. Brongersma[3] and Jennifer A. Dionne[1,4] ✉

Dielectric microcavities with quality factors (*Q*-factors) in the thousands to billions markedly enhance light–matter interactions, with applications spanning high-efficiency on-chip lasing, frequency comb generation and modulation and sensitive molecular detection. However, as the dimensions of dielectric cavities are reduced to subwavelength scales, their resonant modes begin to scatter light into many spatial channels. Such enhanced scattering is a powerful tool for light manipulation, but also leads to high radiative loss rates and commensurately low *Q*-factors, generally of order ten. Here, we describe and experimentally demonstrate a strategy for the generation of high *Q*-factor resonances in subwavelength-thick phase gradient metasurfaces. By including subtle structural perturbations in individual metasurface elements, resonances are created that weakly couple free-space light into otherwise bound and spatially localized modes. Our metasurface can achieve *Q*-factors >2,500 while beam steering light to particular directions. High-*Q* beam splitters are also demonstrated. With high-*Q* metasurfaces, the optical transfer function, near-field intensity and resonant line shape can all be rationally designed, providing a foundation for efficient, free-space-reconfigurable and nonlinear nanophotonics.

Due to their small mode volumes and extremely high quality factors (*Q*-factors), microcavities have transformed both the way we manipulate light and how it is used to interrogate physical systems. Whispering gallery resonators in particular, with *Q*-factors ranging from thousands to billions[1–3], corresponding to resonant lifetimes from picoseconds to microseconds, have produced unprecedented light–matter coupling strengths. For example, whispering gallery resonators including microtoroids and microdroplets have enabled parametric oscillation[4], stimulated Raman scattering[5], cascaded Raman emission[6] and Kerr bistability;[7] while these optical nonlinearities were previously measurable only with ultra-high-power pulsed lasers, high-*Q* cavities made them observable with continuous-wave sources with power levels as low as microwatts. Important devices and applications have also been realized with chip-integrated high-*Q* photonic crystal defect cavities[8] and ring/whispering gallery resonators[9,10], including Raman lasing[11] and nonlinear non-reciprocity[12] with pump thresholds as low as 1 μW, electrically pumped lasing with nA threshold current[13], frequency comb generation[14] and modulation[15], quantum entangled photon generation[16], single-photon switching[17] and isolation[18] and even virus detection at the single-particle level[19].

As the dimensions of an optical cavity are reduced to the subwavelength scale, they take on an entirely different character. In this size regime, resonant modes start to resemble point sources, scattering an incident wave in many different directions[20]. While the large number of scattering channels generally translates into a high radiative loss rate and thus low *Q*-factor, these nanoscale objects, or nanoantennas, have proved to be excellent building blocks for the construction of phase gradient metasurfaces[21–23]. Consisting of non-uniform arrays of nanoscale dielectric or metallic resonators, metasurfaces sculpt the spatial distribution of scattered phase[24], amplitude[25] and polarization[26,27] of an impinging light wave with subwavelength resolution. Such flat optical devices provide a versatile and highly compact route to free-space light manipulation, often meeting or exceeding the performance of their bulk optical counterparts. Unfortunately, the *Q* values of metasurface elements have so far been limited to a few tens. Consequently, nonlinear behaviour has been seen only when pumping the devices with high-power femtosecond pulses[28–30]. Similarly, with weakly resonant scattering being rather insensitive to changes in refractive index, dynamic modulation of phase gradient structures has been difficult; to date, achieving metasurface modulation depths exceeding a few decibels has proved challenging[31,32].

Here, we unveil a new approach combining the power of high-*Q* resonances, seen previously in microcavities, with the full wavefront control enabled by subwavelength diffractive flat optics. By judicious arrangement of isolated silicon nanoantennas supporting specific Mie and guided-mode resonant distributions, we measure *Q*-factors as high as 2,500 in beam-steering and beam-splitting phase gradient metasurfaces. We also numerically extend the concept of high-*Q* beam steering to other spectral transfer functions, including narrowband and slow-light beam steering. In all cases, with silicon having an extinction coefficient $<1\times10^{-9}$ for wavelengths >1.3 μm, the quality factor is limited only by long-range uniformity and lithographic resolution.

Design of guided-mode resonant beam-steering metasurface

Throughout this article, all structures are based on arrays of 600-nm-tall silicon bars atop a sapphire substrate. We will show that this simple platform can be engineered to exhibit unique light-trapping and -scattering properties by combining two distinct design strategies. The first of these relies on the fact that each bar supports a pair of spectrally overlapping electric and magnetic dipole Mie resonances when illuminated with transverse-magnetic-polarized light (Supplementary Fig. 1). This overlap ensures that transmission remains high while the phase delay through a given bar can be varied by adjusting its width (Supplementary Fig. 2). When combined into

---

[1]Department of Materials Science and Engineering, Stanford University, Stanford, CA, USA. [2]Department of Mechanical Engineering, Stanford University, Stanford, CA, USA. [3]Geballe Laboratory for Advanced Materials, Stanford University, Stanford, CA, USA. [4]Department of Radiology, Stanford University, Stanford, CA, USA. [5]Present address: Van der Waals-Zeeman Institute for Experimental Physics, Institute of Physics, University of Amsterdam, Amsterdam, Netherlands. [6]These authors contributed equally: Mark Lawrence, David R. Barton III. ✉e-mail: markl89@stanford.edu; dbarton@stanford.edu; jdionne@stanford.edu

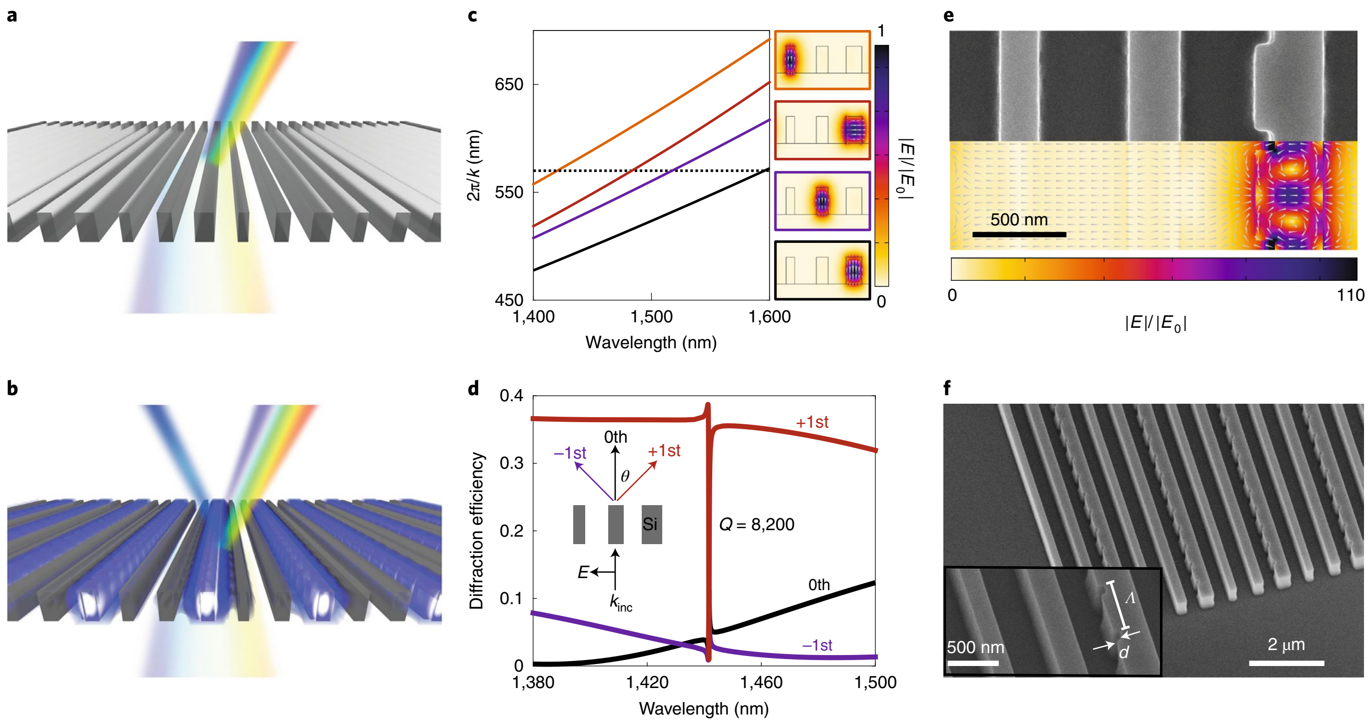

Fig. 1 | Conceptual and numerical design of high-*Q* phase gradient metasurfaces. a, Schematic illustrating broadband beam steering with a Mie resonant phase gradient metasurface. **b**, Schematic illustrating strong light localization and modified diffraction after periodic perturbation of phase gradient metasurface shown in **a**. **c**, Waveguide dispersion for phase gradient metasurface shown in **a**. Left: guided-mode wavelength ($2\pi/k$) plotted against free-space wavelength (λ), with dashed line denoting $2\pi/k = 570$ nm. Right: electric field distributions, colour coded to match dispersion plot. Arrows represent electric field polarization. $|E|/|E_0|$ denotes the amplitude of the electric E field normalized by the incident field amplitude. **d**, Simulated diffraction spectra for periodically perturbed phase gradient metasurface. Inset: schematic showing illumination and diffraction configuration, with k_{inc} representing the incident wavevector and diffraction arrows colour coded to match spectra. Plots of the 0th and −1st orders are reproduced in Supplementary Fig. 4 to better visualize the GMR line shape in these orders. **e**, Top: SEM image of metasurface fabricated with nominal dimensions matching those in **d**. Bottom: simulated electric near-field distribution at the GMR centre wavelength corresponding to that in **d**. Arrows represent electric field polarization. **f**, Angled SEM images, with enlargement in inset, of fabricated phase gradient metasurfaces demonstrating uniform patterning and minimal sidewall tapering. Perturbation period (Λ) and depth (d) are labelled.

a single array, known as a Huygens metasurface[33–35], bars of different width then act as phase 'pixels', collectively generating a desired wavefront for transmitted light. Figure 1a illustrates the optical scattering from a periodic metasurface consisting of three equally spaced nanobars of width 190, 260 and 350 nm, repeated every 2,121 nm. This choice of width corresponds to a constant relative phase delay between neighbouring elements equal to $2\pi/3$, approximating a linear phase gradient (Supplementary Fig. 3). Such a device is known to steer a normally incident beam to the angle θ_t, according to the generalized Snell's law $\theta_t = \arcsin(\lambda/n_t p)$[21], where p is the metasurface period, λ is the free-space wavelength and n_t is the transmission refractive index. In our case, $p = 2{,}121$ nm placing θ_t in the range 40–45° for $\lambda = 1{,}380$–$1{,}500$ nm.

Our second and most important design concept, illustrated schematically in Fig. 1b, involves subtle perturbation of individual nanoantennas to generate high-*Q* dipole resonances. To this end, we note that each nanoantenna maintains a degree of translational symmetry (Fig. 1a). Therefore, in addition to modification of free-space optical signals, each metasurface element can also act as a waveguide. This can be seen from Fig. 1c, which shows the calculated waveguide dispersion for the first four modes within the metasurface. The lowest- and third-lowest-order modes, represented by black and red curves, respectively, correspond to guided solutions of the widest bar (see near fields in Fig. 1c). All these modes possess larger momentum than free-space radiation and so are fully bound to their respective nanoantennas. This momentum mismatch can be bridged by introducing a series of periodic notches, of period Λ. If a sufficient number of notches is used, light will leak back out to free space appearing as a guided-mode resonance (GMR) in the diffraction spectra when Λ equals the guided-mode wavelength[36,37]. This contrasts with grating couplers where, instead, energy leaves through the end of the waveguide. A numerical example of such a resonance, for 100-nm-deep, 100-nm-long notches placed within the largest bar every 570 nm, is given in Fig. 1d. As expected from the phase gradient design, efficient beam steering occurs across most of the plotted spectral range, indicated by the dominance of the +1st diffraction order (red curve). Close to $\lambda = 1{,}440$ nm, a GMR can be seen to interrupt the broadband response, reducing transmission and creating a narrow reflective band. The high *Q*-factor, approximately 8,200, of this resonance indicates that the notch dimensions used represent a weak perturbation to the continuous nanoantenna. In the near field, the long resonant lifetime translates to a field enhancement factor >100 within the perturbed element while the unperturbed elements show little enhancement (Fig. 1e). Unlike most microcavities where the injection efficiency for each mode depends on the specific mode shape, GMRs combine feedback and coupling to the external environment into a single mechanism. This means that, in the absence of parasitic dissipation effects, the conditions for critical coupling are satisfied almost automatically[38]. Importantly for our high-*Q* metasurface design, the absorption losses of silicon in the near infrared are negligible and so the resonant lifetime is dominated by radiative loss; indeed, for small notch depths the radiative loss is entirely dependent on the notch structure. For example, after reproducing Fig. 1d with

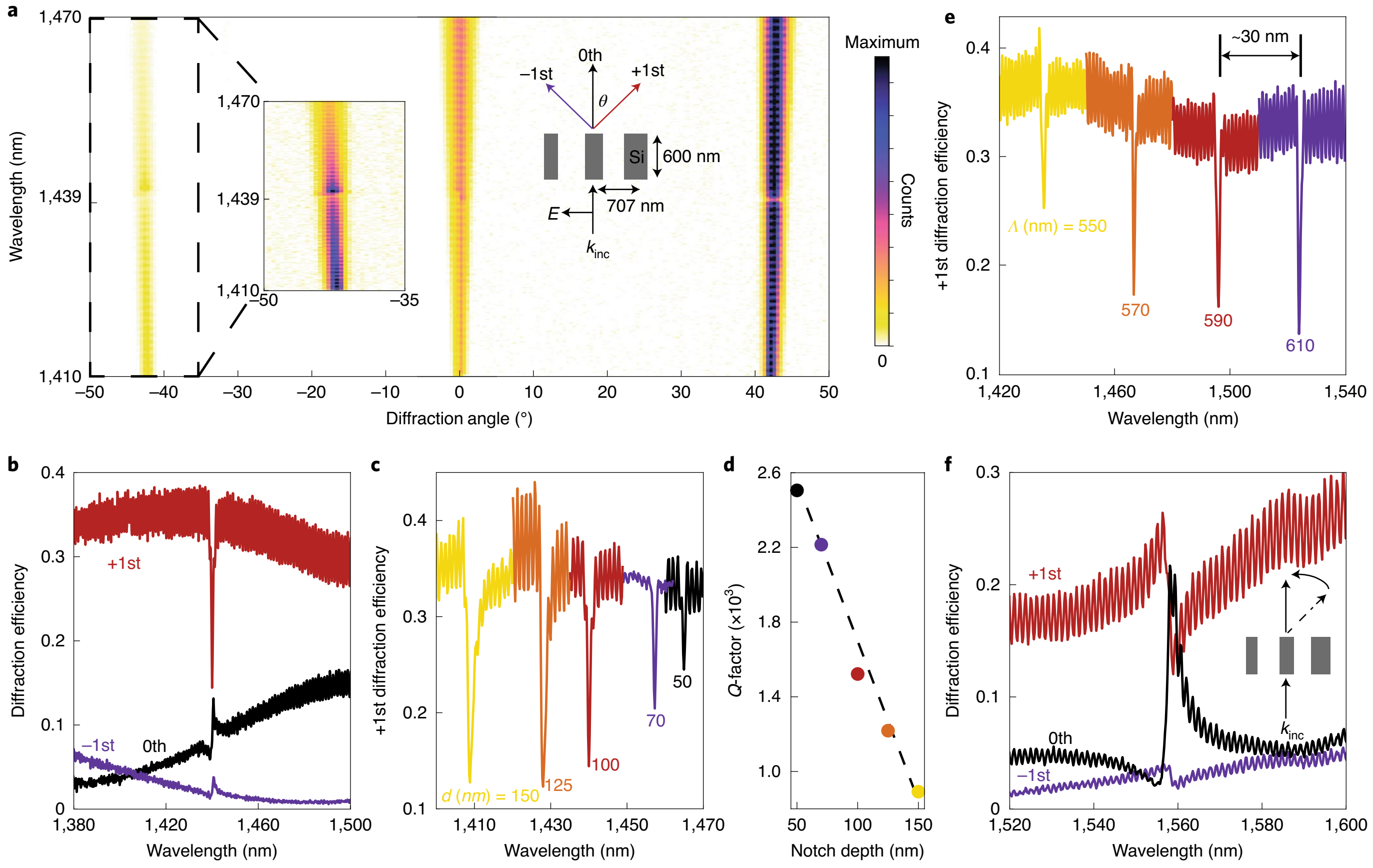

Fig. 2 | Experimental demonstration of high-*Q* phase gradient metasurface beam steering. a, Fourier plane spectral image of beam-steering phase gradient metasurface, with $\Lambda = 570$ nm and $d = 100$ nm. Left inset: enlargement of −1st diffraction order, with value amplified 10×. Right inset: schematic showing illumination and diffraction configuration, with diffraction arrows colour coded to match spectra in **b**. **b**, Diffraction spectra for sample used in **a** and normalized to transmission through the bare substrate, with each diffraction order measured separately. **c**, +1st diffraction spectra for metasurfaces, with perturbation depth d decreasing from 150 to 50 nm and measurement performed as in **b**. **d**, Extracted quality factors from **c**, colour coded to match spectra. The dashed line was drawn as a visual guide. **e**, +1st diffraction spectra for metasurfaces with $d = 70$ nm and varying perturbation period Λ, spanning 550–610 nm in 20-nm increments, with measurements performed as in **b**. Note that the purple curve in **c** and orange curve in **e** are from structures of nominally identical dimensions but were patterned on different samples. Extracted resonant wavelengths for the data in **c**,**e** are included in Supplementary Fig. 9, and extracted quality factors for data in **e** are provided and compared to theory in Supplementary Fig. 10. **f**, Lower-frequency GMR measured in metasurface, with $\Lambda = 570$ nm and $d = 100$ nm and measurements performed as in **b**. Inset schematically compares dominant diffraction on-resonance (solid arrows) and off-resonance (dashed arrow).

the perturbation depth reduced to 50 nm, Q increases to 39,000 (Supplementary Fig. 5). We note that GMRs have previously been investigated in two-dimensionally periodic nanostructures[36,39–41]. In these studies, lattice interference across a one- or two-dimensional grating suppresses free-space scattering, giving rise to very sharp spectral features under free-space illumination. Considerable work has been directed towards locating and implanting these resonances in momentum space, and to understanding the physics governing their formation and collapse[42–45]. Instead, crucially, by not relying simply on modes that are de-localized throughout a two-dimensional plane, our silicon nanobars here maintain a dipole radiation pattern in the plane of diffraction, giving much finer control over scattered wavefronts.

Measurement of high-Q beam steering

Based on the results shown in Fig. 1d, we fabricated a series of phase gradient metasurface samples. A representative scanning electron microscope (SEM) image of one such sample is shown in Fig. 1f, annotated with the two parameters that we varied experimentally—notch depth d and period Λ. We then characterize these devices by illuminating them at normal incidence through the substrate with a collimated white-light laser and measuring transmission with an imaging spectrometer. The Fourier plane spectral map of a metasurface with $\Lambda = 570$ nm and $d = 100$ nm shows strong preferential scattering into the +1st diffraction order with minimal diffraction into other directions, verifying the linear phase gradient design (Fig. 2a). A narrow dip in the +1st diffraction near 1,440 nm reveals the presence of a GMR. This GMR can also be seen to modulate the other two orders, most clearly visible in the inset of Fig. 2a showing a close-up of the −1st diffraction, albeit with a smaller amplitude and distinct line shape. This direction-dependent line shape arises from interference between the weakly coupled waveguide mode and directly transmitted Mie mode, which we will show later allows for diverse functionality. To ensure efficient free-space coupling and reduce finite-size effects, we fabricated metasurfaces of large area ($300 \times 300\,\mu m^2$). We note, however, that the effect does not rely on large areas (Supplementary Fig. 6) and have fabricated metasurfaces of only 7 μm in the phase gradient direction (corresponding to a total of ten metasurface elements) without influencing the high-Q resonant feature (Supplementary Fig. 7).

To better quantify the response of our metasurfaces, we also recorded the real-space spectral image of each diffraction order independently. Using this approach, Fig. 2b shows the normalized spectra from the sample used in Fig. 2a. Apart from the constant

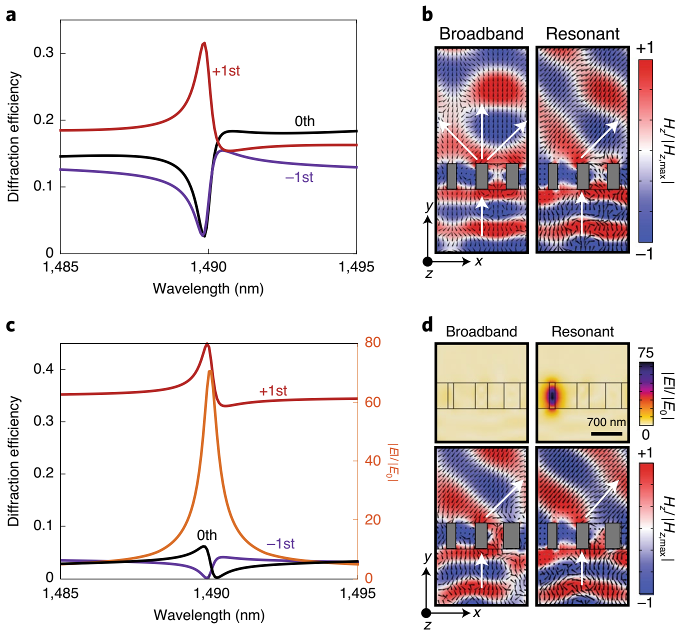

Fig. 3 | Narrowband and slow-light beam steering. a, Simulated diffraction spectra of narrowband beam-steering metasurface with asymmetric perturbations placed in the thinnest bar. Curve colours are chosen to match the schematic in the inset of Fig. 1d. **b**, Magnetic field maps corresponding to **a**, at $\lambda = 1{,}495$ nm (broadband) and $\lambda = 1{,}489.9$ nm (resonant). $H_z/|H_{z,\max}|$ denotes the *z* component of the magnetic *H* field normalized by the maximum field strength. **c**, Simulated diffraction spectra of slow-light beam-steering metasurface, with identical geometry as in **a** for the thinnest bar but different neighbouring bar widths. The orange curve represents peak electric field amplitude (right *y* axis), while remaining curves represent diffraction orders with colours chosen to match the schematic in the inset of Fig. 1d. **d**, Electric field amplitude (top) and magnetic field (bottom) maps corresponding to **c**, at $\lambda = 1{,}495$ nm (broadband) and $\lambda = 1{,}490$ nm (resonant). Shorter arrows overlaid with magnetic fields display the local Poynting vector, while longer arrows highlight the dominant diffraction orders. Detailed metasurface dimensions are given in the text. Colour bar label $|E|/|E_0|$ in **d** denotes the amplitude of the electric *E* field normalized by the incident field amplitude.

oscillations arising from Fabry–Perot resonance in the substrate, we find excellent agreement between Fig. 2b and the numerical data presented in Fig. 1d. A quality factor of 1,500 has been extracted for this mode. In Fig. 2c we fix $\Lambda = 570$ nm and plot relevant portions of the +1st diffraction spectra with the notch depth d swept from 150 nm (yellow curve) to 50 nm (black curve). As d drops to 50 nm we observe a red shift of approximately 60 nm as the GMR approaches the band crossing point of an ideal, or unnotched, waveguide (~1,500 nm) (Fig. 1c). This red shift makes sense, because a smaller perturbation will produce less pronounced Bragg scattering and subsequently less band splitting in guided-mode dispersion (Supplementary Fig. 8). More importantly, from the narrowing line width of the resonant dips in Fig. 2c, as well as the retrieved values plotted in Fig. 2d, Q is seen to increase from 900 to 2,500. This increase clearly demonstrates the strong connection between notch depth and GMR radiative coupling strength. Unfortunately, mode contrast also decreases with decreasing perturbation depth, probably caused by scattering loss. Nevertheless, while lower than numerically predicted due to fabrication imperfections and finite-size effects, our measured values are still two orders of magnitude higher than reported phase gradient metasurface Q values to date. Aside from line width, we also investigated the ability to systematically tune the spectral position of the GMR. Fixing $d = 70$ nm, Fig. 2e displays the relevant portions of the +1st order diffraction efficiency for $\Lambda = 550$ nm (yellow curve) to 610 nm (purple curve), in 20-nm increments. Here, we see that we can shift the resonant centre wavelength by approximately 30 nm for every 20-nm increase in period without substantially impacting the background phase gradient profile.

Since the perturbations are inserted into the largest bar, a second GMR exists at a longer wavelength, corresponding to free-space coupling into a vertically polarized waveguide mode (see the black dispersion curve in Fig. 1c). Figure 2f compares the diffraction spectra of a metasurface near $\lambda = 1{,}560$ nm. As can be seen, the different phase relationship between the broad background and localized mode produces a more asymmetric Fano line shape in the +1st diffraction order[46]. There is little modification to the light scattered into the −1st diffraction order, though there is a marked increase in the 0th order. In other words, on-resonance, the narrowband response is dominated by direct transmission while off-resonance the structure steers light to ~45°.

Narrowband and slow-light beam steering

Having experimentally verified the possibility of embedding high-Q resonances within the diffraction spectrum of a linear phase gradient metasurface, we next explored additional opportunities enabled by this design principle. First, we show how relative weights associated with the available diffraction orders can be independently tailored both on and off resonance. Figure 2f shows that high-Q scattering into the directly transmitted beam can be increased while the first diffracted order is suppressed. This behaviour, which is distinct from the diffraction seen in Fig. 2a–e, arises from the particular symmetry of the GMR and its corresponding radiation pattern. In Fig. 2a–e, the GMR is approximately an in-plane electric dipole (Supplementary Fig. 11). In contrast, the response shown in Fig. 2f is associated with a vertically polarized electric dipole, as seen in the bottom field map in Fig. 1c. When compared to an in-plane dipole, a vertical dipole couples uniquely to both the incident wave and notch symmetry, giving us a new degree of freedom for moulding diffraction. We expect that the behaviour found in Fig. 2b,f will be useful in switching applications where very small optical, electrical or thermal changes to the refractive index can produce large changes in diffraction efficiency.

While the radiation pattern of a GMR depends predominantly on the notch dimensions, the overall metasurface scattering is decided by the interplay between the GMR and the background phase profile. In Fig. 3, we harness this interplay to numerically demonstrate two additional spectral transfer functions of the three-bar design: narrowband beam steering and slow-light beam steering. To achieve these functions, we switch to a vertically polarized electric dipole GMR. We also decrease the width of the notched bar to 210 nm, thereby changing the background Mie scattered phase associated with the narrow resonance, adjusting its line shape. A key property of a vertical electric dipole is that it radiates symmetrically about the vertical axis. This means that such a mode cannot be excited by a plane wave travelling in the vertical direction unless the metasurface breaks that inversion symmetry. In Supplementary Fig. 12 it is seen that the phase of light emitted to the left and right can be controlled by tuning the relative depth of notches placed on the left and right sides of the bar. This allows interference between the resonant scattering and background diffraction to be engineered separately for different diffracted directions. In contrast, the in-plane mode, shown in Supplementary Fig. 11, exhibits very different behaviour with the angular intensity of emission, rather than the angular phase distribution, depending on the notch symmetry.

Taking advantage of these insights, we placed periodic notches of period 635 nm into both sides of the 210-nm-wide bar. The notches were 36-nm deep, 150-nm long on the left (negative x direction)

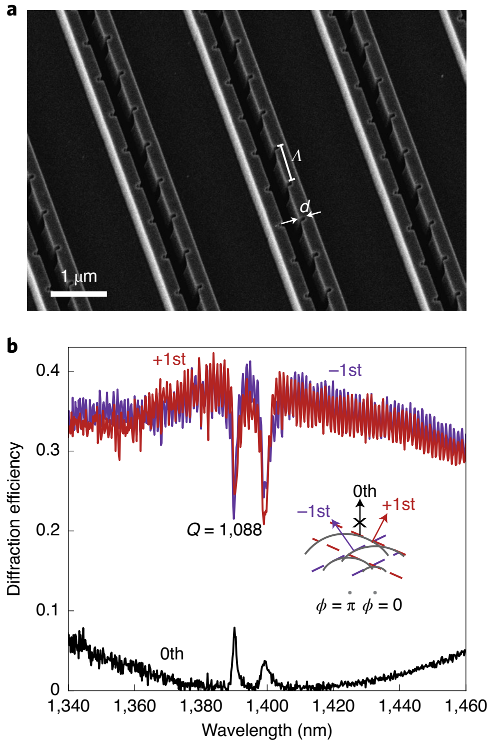

Fig. 4 | High-Q metasurface beam splitter. a, Angled SEM image of a representative beam-splitting metasurface, with annotated perturbation dimensions. **b**, Measured diffraction spectra from metasurface beam splitter with $d = 30$ nm and $\Lambda = 690$ nm. The corresponding Fourier plane spectral map is given in Supplementary Fig. 16. Inset: schematic of working principle of metasurface beam splitter. ϕ denotes the scattered phase of each antenna, grey curves represent crests of cylindrically expanding waves emanating from the antennae and dashed lines highlight plane wavefronts aligned with the diffraction orders, formed from constructive interference between cylindrical waves. Diffraction arrows are colour coded to match spectra.

and 44-nm deep, 150-nm long on the right (positive x direction). We find that placing this structure between bars of width 275 and 280 nm produces sharp dips in both −1st and 0th diffraction orders (Fig. 3a, purple and black curves) but a narrow peak in the +1st diffraction order (Fig. 3a, red curve). As confirmed by the magnetic field profiles and overlaid Poynting vectors (Fig. 3b), this combination results in the metasurface exhibiting balanced diffraction off-resonance but steers the incident wave to ~45° close to the GMR ($\lambda = 1{,}489.9$ nm). In Fig. 3c, we take the structure from Fig. 3a and replace the 275-nm-wide bar with a 370-nm-wide bar. Here, spectral variation in the diffraction around the GMR is almost entirely removed while maintaining the strong spectrally narrow field enhancement associated with high-Q resonance. Similarly, the magnetic field profiles show very little change in the beam-steering response with wavelength, while maps of electric field amplitude reveal a dramatic enhancement (exceeding 75×) within the perturbed bar on-resonance (Fig. 3d). Accordingly, with our high-Q metasurface approach, the optical transfer function, near-field intensity and resonant line shape can all be rationally designed.

High-Q beam splitting

As a general scheme for realizing high-Q phase gradient metasurfaces, structures can easily be designed with wavefront-shaping capabilities beyond 45° beam steering. For example, changing the metasurface supercell period while maintaining the linear phase gradient can alter the steering angle. Supplementary Fig. 13 shows a suite of samples engineered to steer light to 36°, with high-Q responses similar to those shown in Fig. 2. Figure 4 shows an experimental demonstration of free-space high-Q metasurface beam splitting. In this case, light incident on the metasurface is redirected in approximately equal magnitude to the +1 and −1 diffraction orders while cancelling the 0th-order transmission almost entirely. An angle-view SEM image of one such fabricated structure is shown in Fig. 4a. The metasurface has the same phase gradient period (2,121 nm) as the 45° beam-steering samples and is composed of two phase pixels. One pixel consists of a nanoantenna made from two coupled 240-nm-wide silicon nanobars. Light leaking through the bare substrate between nanoantennas acts as the second pixel. Measured spectra from a beam-splitting metasurface, shown in Fig. 4b, reveal balanced diffraction in the +1st (red curve) and −1st (purple curve) directions, while the 0th-order transmission (black curve) is almost entirely suppressed at the centre wavelength of 1,400 nm. A schematic representation of the working principle underlying beam splitting is shown in the inset of Fig. 4b, and numerically in Supplementary Fig. 14. With neighbouring pixels differing in their phase delay by π, destructive interference occurs in the forward direction while constructive interference occurs for waves deflected to ~±41°.

Unlike our other, beam-steering devices, the guided modes of the metasurface pictured in Fig. 4a are not localized within a single nanobar. Instead, coupling between the bars generates a collection of even and odd waveguide modes (Supplementary Fig. 15). Following our previous prescription, we pattern the inside edge of each element with 80-nm-long perturbations of period $\Lambda = 690$ nm and depth d (in Fig. 4a, $d = 100$ nm to best visualize the structure; in Fig. 4b the notch depth is 30 nm). Two sharp GMRs appear in the diffraction spectra of Fig. 4b at wavelengths 1,389 and 1,398 nm with Q of 1,088 and 580, respectively (see Supplementary Fig. 17 for top-down SEM images and a parameter sweep of perturbation geometries). Here, the beam-splitting efficiency is reduced while direct transmission is resonantly increased. Varying perturbation depth, as before, modifies the Q-factor (see Supplementary Fig. 17). Note that although four guided modes exist for this period in this spectral range, by maintaining inversion symmetry in the diffraction plane only the two antisymmetric GMRs can be excited with the polarization we use for illumination (see Supplementary Fig. 18).

Conclusions

While nanoantennas represent an exciting development for optical science, researchers typically face a trade-off between antenna size in relation to wavelength and resonant lifetime. In shaping diffraction using high-Q nanoantennas of subwavelength cross-section in the diffraction plane, we provide experimental evidence to suggest that this trade-off may not, in fact, be fundamental. These results point to the possibility that highly resonant and highly compact features, once in the purview only of on-chip photonics, can be rationally designed to coincide with an arbitrarily chosen electromagnetic wavefront. Our proof-of-principle phase gradient metasurfaces, namely beam steerers and beam splitters, can lead to a host of high-Q diffractive flat optics including lenses[47] and holograms. We also demonstrated that diffraction order-dependent GMR dispersion can be controlled via the perturbation symmetry and that multiplexing can be achieved using coupled elements. The phenomenon we present is not exclusive to nanobars of varying width—we expect to find similar behaviour in other design strategies, including isotropic structures and those based on geometric phase. The present study has focused on devices that maintain periodicity along one dimension and thus require sufficient spatial extent in that direction to sustain long resonant lifetimes. This, however, is not an essential requirement. By both reducing group velocity dispersion of the guided modes with high-contrast index variations and using photonic crystal mirrors to reflect light that would otherwise leak through the ends of the nanoantennas, the scale of our metasurfaces can be reduced considerably. We note that our highest measured Q (~2,500) is limited mainly by scattering losses. Much higher Q-factors (10^4–10^5) should be achievable with refined fabrication processes and improved imperfection-tolerant designs. By enabling resonant near-field intensity and line shape to be engineered in conjunction with arbitrary wavefront transformations, we envision an impact by high-Q phase gradient metasurfaces on any discipline that benefits from efficient diffractive optical switching or tuning and low nonlinear thresholds. Specific applications include light detection and ranging (for example LIDAR), light fidelity (LiFi), and quantum and non-reciprocal optical communication.

Online content

Any methods, additional references, Nature Research reporting summaries, source data, extended data, supplementary information, acknowledgements, peer review information; details of author contributions and competing interests; and statements of data and code availability are available at https://doi.org/10.1038/s41565-020-0754-x.

Received: 7 January 2020; Accepted: 7 July 2020;

References

1. Armani, D. K., Kippenberg, T. J., Spillane, S. M. & Vahala, K. J. Ultra-high-Q toroid microcavity on a chip. *Nature* **421**, 925–928 (2003).
2. Gorodetsky, M. L., Savchenkov, A. A. & Ilchenko, V. S. Ultimate Q of optical microsphere resonators. *Opt. Lett.* **21**, 453–455 (1996).
3. Vernooy, D. W., Ilchenko, V. S., Mabuchi, H., Streed, E. W. & Kimble, H. J. High-Q measurements of fused-silica microspheres in the near infrared. *Opt Lett* **23**, 247–249 (1998).
4. Kippenberg, T. J., Spillane, S. M. & Vahala, K. J. Kerr-nonlinearity optical parametric oscillation in an ultrahigh-Q toroid microcavity. *Phys. Rev. Lett.* **93**, 083904 (2004).
5. Lin, H.-B., Eversole, J. D. & Campillo, A. J. Continuous-wave stimulated Raman scattering in microdroplets. *Opt. Lett.* **17**, 828–830 (1992).
6. Min, B., Kippenberg, T. J. & Vahala, K. J. Compact, fiber-compatible, cascaded Raman laser. *Opt. Lett.* **28**, 1507–1509 (2003).
7. Treussart, F. et al. Evidence for intrinsic Kerr bistability of high-Q microsphere resonators in superfluid helium. *Eur. Phys. J. D* **1**, 235–238 (1998).
8. Akahane, Y., Asano, T., Song, B. S. & Noda, S. High-Q photonic nanocavity in a two-dimensional photonic crystal. *Nature* **425**, 944–947 (2003).
9. Lee, H. et al. Chemically etched ultrahigh-Q wedge-resonator on a silicon chip. *Nat. Photonics* **6**, 369–373 (2012).
10. Lin, G., Diallo, S., Henriet, R., Jacquot, M. & Chembo, Y. K. Barium fluoride whispering-gallery-mode disk-resonator with one billion quality-factor. *Opt. Lett.* **39**, 6009–6012 (2014).
11. Takahashi, Y. et al. A micrometre-scale Raman silicon laser with a microwatt threshold. *Nature* **498**, 470–474 (2013).
12. Peng, B. et al. Parity–time-symmetric whispering-gallery microcavities. *Nat. Phys.* **10**, 394–398 (2014).
13. Ellis, B. et al. Ultralow-threshold electrically pumped quantum-dot photonic-crystal nanocavity laser. *Nat. Photonics* **5**, 297–300 (2011).
14. Stern, B., Ji, X., Okawachi, Y., Gaeta, A. L. & Lipson, M. Battery-operated integrated frequency comb generator. *Nature* **562**, 401–405 (2018).
15. Wang, C. et al. Monolithic lithium niobate photonic circuits for Kerr frequency comb generation and modulation. *Nat. Commun.* **10**, 978 (2019).
16. Guo, X. et al. Parametric down-conversion photon-pair source on a nanophotonic chip. *Light Sci. Appl.* **6**, e16249 (2017).
17. Sun, S., Kim, H., Luo, Z., Solomon, G. S. & Waks, E. A single-photon switch and transistor enabled by a solid-state quantum memory. *Science* **361**, 57–60 (2018).
18. Scheucher, M., Hilico, A., Will, E., Volz, J. & Rauschenbeutel, A. Quantum optical circulator controlled by a single chirally coupled atom. *Science* **354**, 1577–1580 (2016).
19. Vollmer, F., Arnold, S. & Keng, D. Single virus detection from the reactive shift of a whispering-gallery mode. *Proc. Natl Acad. Sci. USA* **105**, 20701–20704 (2008).
20. Kuznetsov, A. I., Miroshnichenko, A. E., Brongersma, M. L., Kivshar, Y. S. & Luk'yanchuk, B. Optically resonant dielectric nanostructures. *Science* **354**, aag2472 (2016).
21. Yu, N. et al. Light propagation with phase discontinuities: generalized laws of reflection and refraction. *Science* **334**, 333–337 (2011).
22. Yu, N. & Capasso, F. Flat optics with designer metasurfaces. *Nat. Mater.* **13**, 139–150 (2014).
23. Lin, D., Fan, P., Hasman, E. & Brongersma, M. L. Dielectric gradient metasurface optical elements. *Science* **345**, 298–302 (2014).
24. Zheng, G. et al. Metasurface holograms reaching 80% efficiency. *Nat. Nanotechnol.* **10**, 308–312 (2015).
25. Liu, L. et al. Broadband metasurfaces with simultaneous control of phase and amplitude. *Adv. Mater.* **26**, 5031–5036 (2014).
26. Balthasar Mueller, J. P., Rubin, N. A., Devlin, R. C., Groever, B. & Capasso, F. Metasurface polarization optics: independent phase control of arbitrary orthogonal states of polarization. *Phys. Rev. Lett.* **118**, 113901 (2017).
27. Yin, X., Ye, Z., Rho, J., Wang, Y. & Zhang, X. Photonic spin hall effect at metasurfaces. *Science* **339**, 1405–1407 (2013).
28. Li, G. et al. Continuous control of the nonlinearity phase for harmonic generations. *Nat. Mater.* **14**, 607–612 (2015).
29. Almeida, E., Shalem, G. & Prior, Y. Subwavelength nonlinear phase control and anomalous phase matching in plasmonic metasurfaces. *Nat. Commun.* **7**, 10367 (2016).
30. Wang, L. et al. Nonlinear wavefront control with all-dielectric metasurfaces. *Nano Lett.* **18**, 3978–3984 (2018).
31. Wu, P. C. et al. Dynamic beam steering with all-dielectric electro-optic III–V multiple-quantum-well metasurfaces. *Nat. Commun.* **10**, 3654 (2019).
32. Li, S. Q. et al. Phase-only transmissive spatial light modulator based on tunable dielectric metasurface. *Science* **364**, 1087–1090 (2019).
33. Decker, M. et al. High-efficiency dielectric Huygens' surfaces. *Adv. Opt. Mater.* **3**, 813–820 (2015).
34. Pfeiffer, C. et al. Efficient light bending with isotropic metamaterial Huygens' surfaces. *Nano Lett.* **14**, 2491–2497 (2014).
35. Estakhri, N. M. & Alù, A. Wave-front transformation with gradient metasurfaces. *Phys. Rev. X* **6**, 041008 (2016).
36. Wang, S. S. & Magnusson, R. Theory and applications of guided-mode resonance filters. *Appl. Opt.* **32**, 2606–2613 (1993).
37. Lawrence, M., Barton, D. R. & Dionne, J. A. Nonreciprocal flat optics with silicon metasurfaces. *Nano Lett.* **18**, 1104–1109 (2018).
38. Jiang, X. et al. Chaos-assisted broadband momentum transformation in optical microresonators. *Science* **358**, 344–347 (2017).
39. Fan, S. & Joannopoulos, J. D. Analysis of guided resonances in photonic crystal slabs. *Phys. Rev. B* **65**, 235112 (2002).
40. Wu, C. et al. Spectrally selective chiral silicon metasurfaces based on infrared Fano resonances. *Nat. Commun.* **5**, 3892 (2014).
41. Yang, Y., Kravchenko, I. I., Briggs, D. P. & Valentine, J. All-dielectric metasurface analogue of electromagnetically induced transparency. *Nat. Commun.* **5**, 5753 (2014).
42. Wei Hsu, C. et al. Observation of trapped light within the radiation continuum. *Nature* **499**, 188–191 (2013).
43. Kodigala, A. et al. Lasing action from photonic bound states in continuum. *Nature* **541**, 196–199 (2017).
44. Ha, S. T. et al. Directional lasing in resonant semiconductor nanoantenna arrays. *Nat. Nanotechnol.* **13**, 1042–1047 (2018).
45. Yang, Y. et al. Nonlinear fano-resonant dielectric metasurfaces. *Nano Lett.* **15**, 7388–7393 (2015).
46. Limonov, M. F., Rybin, M. V., Poddubny, A. N. & Kivshar, Y. S. Fano resonances in photonics. *Nat. Photonics* **11**, 543–554 (2017).
47. Klopfer, E., Lawrence, M., Barton, D. R., Dixon, J. & Dionne, J. A. Dynamic focusing with high-quality-factor metalenses. *Nano Lett.* **20**, 5127–5132 (2020).

Methods

Design. Sample dimensions were designed using COMSOL Multiphysics to model both waveguide dispersion and phase response. The phase response to determine each meta-element was designed using periodic boundary conditions with a silicon bar of given dimensions.

Fabrication. The metasurfaces were fabricated using standard lithographic procedures. First, 600-nm, single-crystal silicon-on-sapphire (MTI Corp.) substrates were cleaned by sonication in acetone and isopropyl alcohol. Following a dehydration bake, HSQ negative tone resist (XR-1541–06, Corning) was spin-coated to the sample and baked for 45 min at 90 °C. To reduce charging, a charge dissipation layer was applied (e-spacer, Showa Denko) and the sample was baked again. The patterns were written using electron-beam lithography (Jeol 6300-FS) and developed in strong base. Following lithography, the pattern was transferred to the silicon layer using reactive ion etching. First, a non-selective etch was performed to break through the native oxide while the main etch step utilized Cl_2, HBr and O_2 (Lam TCP 9400), etching anisotropically and stopping on the sapphire substrate. The resist was stripped using 2% hydrofluoric acid in water, following an organic clean using a Piranha solution heated to 120 °C.

Characterization. Representative images were taken using a FEI Magellan 400 XHR scanning electron microscope with a field emission gun source or FEI Helios 600i dual-beam SEM/FIB. For top-down images, a conductive polymer (ESPACER) was applied to reduce charging in the images. For side and tilted views, a representative sample was coated with a ~3.5-nm film of Au/Pd to reduce charging. Images were typically acquired with accelerating voltage 2–5 kV.

Optical characterization. Spectroscopic measurements were made using a home-built, angle-resolved microscope (Supplementary Fig. 19). A collimated broadband laser (NKT supercontinuum) was polarized and weakly focused onto the metasurface at normal incidence. Illumination was perpendicular to the metasurface on an assembly that can set a vertical incident angle relative to the objective. Insertion of a Bertrand lens on a flip mount focused on the back focal plane of the objective allowed projection of the Fourier plane onto a camera. Because the metasurface diffracts in one plane, we use a grating to split the spectral response in the other dimension and thereby we simultaneously obtain the energy and momentum of the transmitted light. Light is collected with a 0.42-numerical aperture objective (at a half-angle of 24°). To capture all three diffraction orders, we performed two measurements with the sample/illumination angle set to ±20° relative to the objective. One measurement contains the 0th and +1st diffraction orders while the other contains the 0th and −1st. The two spectral maps are aligned, and overlapping data are removed (Fig. 2a). Throughout the paper the resonant spectral features were analysed by fitting the diffraction efficiency data with the function

$$T = \left|\frac{1}{1 + F\sin^2(n_s k h_s)}\right| \left|a_r + a_i i + \frac{b}{f - f_0 + \gamma i}\right|^2 \quad (1)$$

The second multiplicative term represents the superposition between a constant complex background, $a_r + a_i i$, and a Lorentzian resonance with resonant frequency f_0 and full-width at half-maximum 2γ. The Q-factor of this resonance is then taken to be $Q = f_0/2\gamma$. The first term accounts for the Fabry–Perot interference through the substrate of thickness h_s and refractive index n_s. k is the free-space wavevector ($2\pi/\lambda$) and F accounts for the reflectivity of the air–substrate interfaces.

Data availability

The data that support the plots within this paper and other findings of this study are available from the corresponding authors on reasonable request.

Acknowledgements

We thank R. Tiberio and U. Raghuram for helpful discussions regarding fabrication. This work was supported by PECASE (grant no. FA9550-15-10006) and NSF EFRI (grant no. 1641109). The device fabrication, performed in part by J.D., was supported by the DOE 'Photonics at Thermodynamic Limits' Energy Frontier Research Center under grant no. DE-SC0019140. J.v.d.G, J.-H.S. and M.L.B. acknowledge funding from an individual investigator grant from AFOSR (no. FA9550-18-1-0323). Part of this work was performed at the Stanford Nano Shared Facilities and Stanford Nanofabrication Facilities, which are supported by the National Science Foundation and National Nanotechnology Coordinated Infrastructure under award no. ECCS-1542152.

Author contributions

M.L., D.R.B. and J.D. conceived the idea. M.L. performed full-field simulations. D.R.B., J.D. and J.v.d.G. fabricated the devices. M.L. and J.-H.S. conducted optical characterization. D.R.B. and M.L. wrote the manuscript. J.A.D. supervised the project, along with M.L.B. on the relevant portions of the research. All authors contributed to preparation of the manuscript.

Competing interests

The authors declare no competing interests.

Additional information

Supplementary information is available for this paper at https://doi.org/10.1038/s41565-020-0754-x.

Correspondence and requests for materials should be addressed to M.L., D.R.B. or J.A.D.

Peer review information *Nature Nanotechnology* thanks Lan Yang and the other, anonymous, reviewer(s) for their contribution to the peer review of this work.

Reprints and permissions information is available at www.nature.com/reprints.